



Cite this: *Mater. Adv.*, 2022,
3, 2123

Influence of pH-neutral lithium polystyrenesulfonate polyelectrolyte on the energy band structure and performance of organic solar cells†

Merve Nur Ekmekci,^a Ju Hwan Kang, ^a Yeasin Khan,^{ab} Jung Hwa Seo ^{*a} and Bright Walker ^{*b}

Poly(3,4-ethylenedioxythiophene):polystyrene sulfonate (PEDOT:PSS) is used ubiquitously in organic solar cell (OSC) devices, however, it is not clear how the anionic PSS component by itself affects the band structure of OSCs. In this contribution, we've conducted a detailed investigation of the pH-neutral lithium salt of PSS (Li:PSS) and mixtures of Li:PSS with PEDOT:PSS and their effect on the energy band structure and performance of OSCs. There is currently a need for transparent and pH neutral hole transport layer (HTL) materials in the context of OSCs, and Li:PSS itself is a solution-processable, transparent and pH-neutral polyelectrolyte that was found to function as an HTL in OSCs as a thin interfacial layer. Atomic force microscopy measurements reveal smooth films with reduced root-mean-square roughness compared to PEDOT:PSS. Electronic band structures at the interface between Li:PSS based HTLs and the active layer were determined and compared to PEDOT:PSS, revealing low hole injection barriers and a p-type band in the active layer at the HTL interface. These effects are consistent with the improved current density and high efficiency (up to 8.33%) observed in devices using mixtures of Li:PSS and PEDOT:PSS.

Received 30th September 2021,
Accepted 1st January 2022

DOI: 10.1039/d1ma00913c

rsc.li/materials-advances

Introduction

Solar cells are one of the most environmentally conscientious methods of producing electricity due to the practically limitless energy produced by the sun along with their low maintenance and lack of pollution after being installed. In the context of renewable energy sources, organic solar cells (OSCs) are an emerging technology with comparatively easy device fabrication requirements and excellent potential for mass-production.^{1,2} Like other solar cells, OSCs generate electrical energy *via* absorption of sunlight in their active layers,^{3–5} and efficient devices incorporate interfacial layers such as electron transport layers (ETLs) or a hole transport layer (HTL) adjacent to the active layer to extract negative and positive charges, respectively, with minimal losses. Like the active layers in OSCs, it is desirable for HTLs and ETLs to be based on economical and solution-processable materials and new materials and architectures are constantly being developed.⁶

Increasing interest in organic solar cells has driven remarkable advances in the discovery of new materials and devices with high-performance architectures; a wide array of new HTL and ETL materials have emerged in the past few years and contributed to improvements in device efficiency.^{7,8} Compared to the wide variety of ETLs that have been reported, a comparatively limited number of HTL types are known to be effective in conventional structure OSCs.⁹

Poly(3,4-ethylenedioxythiophene):polystyrene sulfonate (PEDOT:PSS) is most often used as an HTL in conventional structure OSCs.^{10–12} It has several advantages including water solubility, facile solution processability and low-temperature fabrication.¹³ However, the material possesses both advantages and disadvantages. Its work function (WF) is not high enough for many active layers^{14–16} and may lead to recombination losses at the anode. Additionally, it has an acidic nature¹⁷ and low transparency which leads to decreased light absorption in the active layer and reduced current density. The acidic surface can damage the active layer surface in contact with PEDOT:PSS^{18,19} and also may corrode the transparent, indium tin oxide (ITO) electrode.²⁰

These disadvantages highlight the need for an improved alternative.²¹ Several alternative HTL materials have been investigated, however, the performance of alternative HTLs has generally lagged behind PEDOT:PSS. For instance, one of

^a Department of Semiconductors and Chemical Engineering (BK21 FOUR), Dong-A University, Busan, 49315, Republic of Korea. E-mail: seojh@dau.ac.kr

^b Department of Chemistry, Kyung Hee University, Seoul, 02453, Republic of Korea. E-mail: walker@khu.ac.kr

† Electronic supplementary information (ESI) available. See DOI: 10.1039/d1ma00913c



the most successful HTLs called “CPE-K” has yielded up to 8.0% PCE in poly [[4,8-bis[(2-ethylhexyl)oxy]benzo[1,2-*b*:4,5-*b*]dithiophene-2,6-diyl][3-fluoro-2-[(2-ethylhexyl) carbonyl thieno[3,4-*b*]thiophenediyl]] (PTB7) based devices using MeOH/Ca/Al as a cathode. Due to its homogeneous conductivity and pH neutrality, it showed a better performance than PEDOT:PSS.²² Besides conjugated polyelectrolytes, metal oxides such as NiO_x , MoO_3 and V_2O_5 have been used successfully as HTLs.^{23–27} However, only the power conversion efficiencies (PCEs) of MoO_3 devices have been consistently greater than PEDOT:PSS. Graphene oxides (GOs) used below PEDOT:PSS have been reported.^{28–31} These devices together with PEDOT:PSS have yielded efficiencies of up to 7.1% over the years with different active layer compositions. Additionally, copper sulfide (CuS), copper bromide (CuBr) and nickel sulphide (NiS) have been studied as solution-processable HTLs in conventional device architectures.^{32–34} Efficiencies of these inorganic HTLs were reported as 4.32% and 5.07%, respectively.

Recently, there have been reports of solution-processable anodic buffer layers, alone and in combination with PEDOT:PSS.³⁵ Even though these materials were able to exhibit higher WFs than PEDOT:PSS, they have not often been able to produce higher efficiencies.

In this work, we investigate the role of the anionic polyelectrolyte, PSS, in OSC HTLs using the relatively inert Li^+ salt of PSS (Li:PSS) and mixtures of this pH-neutral polyelectrolyte with PEDOT:PSS. This study explores the effect of Li:PSS on the characteristics of HTLs comprising Li:PSS and Li:PSS/PEDOT:PSS mixtures, their effect on the electronic band structure of OSC devices at the Li:PSS/PTB7 interface and ultimately, on OSC performance and stability. From the measured energy level alignment, critical parameters of OSCs such as hole injection barrier, electron injection barrier, and the presence or absence of p-type doping and band-bending were quantified to achieve a detailed understanding of OSC behavior with these interlayers.

Experimental details

Li:PSS synthesis

Li:PSS was prepared by the reaction between Li_2CO_3 (0.60 g, 3.25 mmol) and a commercial solution of polystyrene sulfonic acid (HPSS, Aldrich, 75 kD molecular weight (MW), 3 mmol based on the monomer MW). Briefly, Li_2CO_3 was dispersed in 2 ml H_2O in a 10 ml vial with a magnetic stir bar and HPSS was slowly added, causing the mixture to bubble vigorously consistent with the release of CO_2 . After the bubbles stopped, the mixture was shaken vigorously and allowed to stand overnight. The solution was filtered through a 0.45 μm cellulose acetate syringe filter and precipitated into isopropanol (IPA). Several drops of hexane were added to help break the milky colloid which formed. The mixture was centrifuged, and the supernatant liquid discarded. The polymer was re-dissolved in 10 ml of methanol and filtered through a 0.45 μm PTFE filter to remove excess unreacted Li_2CO_3 . The clear solution was precipitated into ethyl acetate, hexane was added to help break the

milky colloid, and a small amount of solid polymer separated upon centrifuging the colloid. The precipitated polymer was washed with IPA and hexane, then dried in a nitrogen glove box. The pH of a solution (2.1 mg/5 ml H_2O) was 7.2. 75 mg was recovered.

Device fabrication (conventional structure)

ITO substrates were cleaned in deionized water, acetone, and IPA respectively by ultra-sonication for 20 minutes each. The ITO substrates were further cleaned by UV-ozone treatment for 10 minutes to remove trace organic residue and dried in an oven at 80 °C overnight. Conventional OSCs were fabricated on the ITO substrates by sequentially depositing an HTL, active layer and ETL respectively and the Al electrodes. HTLs were deposited by spin coating different HTL solutions for 30 seconds at 2000 rpm. For single-layer solutions, Li:PSS was prepared in methanol with different concentrations (0.005–0.035 wt%), spin-coated and dried on a hot plate for 10 minutes at 80 °C. Li:PSS mixtures with PEDOT:PSS were also investigated. Table S1 in the ESI† describes the composition of each HTL used in this study. In all cases, solutions were prepared by diluting with deionized water as PEDOT:PSS is a water-based solution. Mixed Li:PSS/PEDOT:PSS HTLs were spin cast using mixed solutions as described and dried on a hot plate in air at 120 °C. After HTL deposition, samples were brought inside a nitrogen-filled glove box and all subsequent fabrication steps were carried out in the absence of air. Bulk heterojunction active layer solutions were prepared one night before and allowed to stir at 45 °C on a hot plate over-night. PTB7:[6,6]-phenyl-C71-butyric acid methyl ester (PC₇₁BM) solutions (1:1.5 ratio) were prepared in chlorobenzene solvent with a 3% DIO additive.³⁶ These were spin-coated on top of the HTLs at 1300 rpm for 45 seconds and dried for 10 minutes on a hot plate at 80 °C. Then, ETLs comprising poly(9,9-bis(3'-(*N,N*-dimethyl)-*N*-ethylammonium-propyl-2,7-fluorene)-*alt*-2,7-(9,9-dioctylfluorene))dibromide (PFN⁺Br[−]) (Sigma, 0.1 wt%) were deposited using solutions in methanol solvent and spin-coated at 2000 rpm for 40 seconds. The films were dried for 10 minutes on a hot plate at 60 °C.^{37,38} Finally, the devices were transferred to a vacuum chamber and Al cathodes (100 nm) were deposited by thermal evaporation under vacuum (about 10^{−6} Torr).

Characterization

Current density–voltage (*J*–*V*) measurements were collected using a Keithley 2635 source measure unit inside a nitrogen-filled glove-box using a high-quality optical fiber to guide the light from a xenon arc lamp to the solar cell devices. The solar cell devices were illuminated with a light intensity of 100 mW cm^{-2} calibrated using a standard silicon reference cell immediately prior to testing. External quantum efficiency (EQE) measurements were carried out using a QEX7 system manufactured by PV Measurements, Inc. Atomic force microscopy (AFM) images were obtained using an INOVA Multimode microscope operating in tapping mode. Ultraviolet and X-ray photoelectron spectroscopy (UPS and XPS, respectively) spectra were obtained using a Thermo Fischer Scientific ESCALB 250XI.



Results and discussion

One of the motivations to explore Li:PSS as an HTL material is due to its reduced acidity compared to PEDOT:PSS, which is ubiquitously used in conventional structure OSCs. We anticipated that the reduced acidity of Li:PSS would prolong the stability of OSCs by eliminating acid-mediated degradation mechanisms which are known to occur at the interface between an HTL and active layer in typical OSCs. Fig. S1a of the ESI[†] illustrates the results of pH paper tests for all of the different types of HTL solutions used in this study. The pH of PEDOT:PSS was measured to be 1.21, which is sufficiently acidic to damage ITO over time, whereas the pH of a 0.005 wt% Li:PSS solution was 6.36, close to the pH of the de-ionized water used to make it (6.80) and very close to neutral. The pH of Li:PSS mixtures ranged from 1.50 (for “Li:PSS M70”; 70% PEDOT:PSS) to 2.53 (“Li:PSS M10”; 10% PEDOT:PSS). Using small amounts of PEDOT:PSS as an additive in Li:PSS resulted in pH values ranging from 2.39 (for “Li:PSS A16”; 13.8% PEDOT:PSS) to 4.13 (for “Li:PSS A1”; lower than 1% PEDOT:PSS). Thus, the pH became more neutral as the proportion of Li:PSS increased and as the proportion of PEDOT:PSS decreased. A summary of pH values and WFs (taken from UPS data, discussed in detail later) is seen in Fig. 1, and a table of compositions and their measured pH values, as well as pictures of the pH test strips used for each solution, are included in the ESI[†] (Table S1 and Fig. S1(a), respectively, ESI[†]). It has been reported in the literature³⁹ that acidic HTLs have a higher WF at their surfaces than non-acidic HTLs, however, we observed that the WF values for Li:PSS and all combinations of Li:PSS and PEDOT mixtures were in the range of 4.86 to 4.94 eV, similar, or slightly lower than the value measured for PEDOT:PSS (5.01).

To investigate the effect of acidity on the stability of PTB7 films, we monitored the absorption of PTB7 films in different environments with variable acidity. PTB7 films become bleached and transparent as they degrade over time. The relationship between pH values and time-dependent degradation of PTB7 thin films was investigated by UV-visible absorbance spectroscopy (Fig. S1(b)–(e), ESI[†]). We observed that the visible absorbance of PTB7 decreased with decreasing pH values due to chemical degradation of the conjugated π -system in the polymer. To quantify the degradation, the intensity of the maximum absorption band at 705 nm was

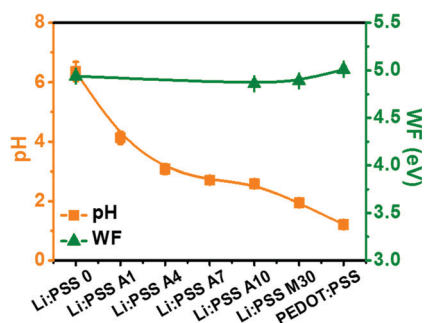


Fig. 1 pH values and work functions of Li:PSS and mixtures with PEDOT:PSS in various proportions.

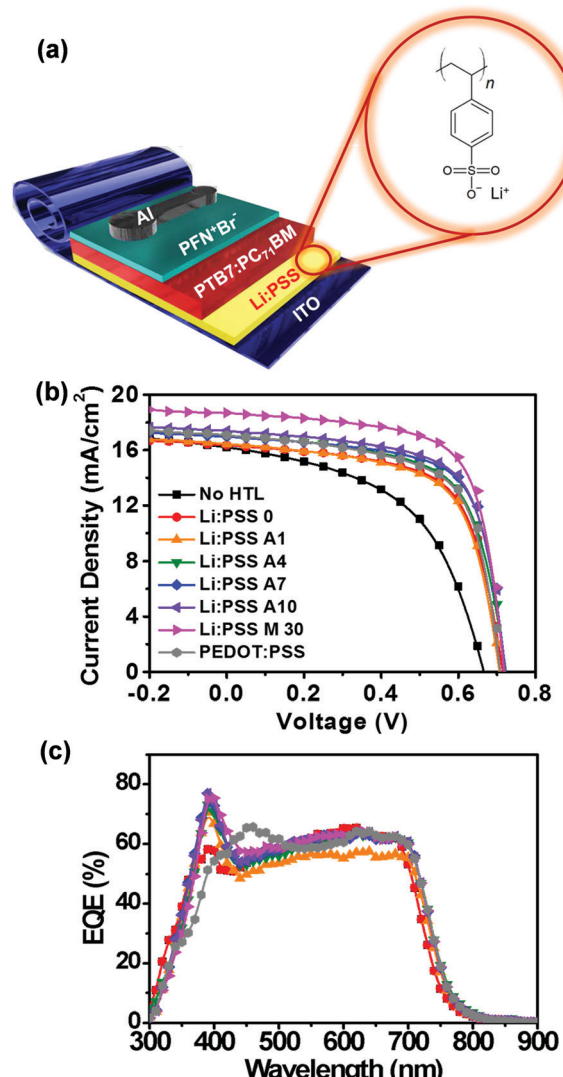


Fig. 2 (a) Device architecture of conventional OSCs with ITO/Li:PSS/PTB7:PC₇₁BM/PFN⁺Br⁻/Al and the chemical structure of Li:PSS, (b) J-V curves of PTB7:PC₇₁BM OSCs measured under simulated AM 1.5G solar light and (c) EQE spectra.

monitored over time. PTB7 films on glass substrates exposed to ambient air lost 23.3% of their original optical density after 4 weeks (27 days). When the PTB7 films were immersed in 2 M HCl, they completely degraded (0% of their original absorption) within only 3 days illustrating the instability of PTB7 to acid. Commercial PEDOT:PSS contains a significant proportion of styrene sulfonic acid groups. We compared the degradation of PTB7 exposed to dilute polystyrene sulfonic acid (H:PSS) and Li:PSS solutions with the same concentration; exposure to a 0.1 wt% HPSS solution (5.4 mM) caused the films to lose 84.0% of their original optical density over 27 days, while exposure to 0.1 wt% Li:PSS resulted in only a 54.4% decrease in optical density, showing that Li:PSS solutions are much less deleterious to PTB7 films than HCl or HPSS, which is present in PEDOT:PSS.

Similar experiments were carried out with PTB7 films deposited on solid films of ITO, PEDOT:PSS, H:PSS and Li:PSS.



Table 1 Device parameters of OSCs with HTLs consisting of Li:PSS and mixtures of Li:PSS with PEDOT:PSS

HTL	J_{SC} (mA cm $^{-2}$)	Spectral J_{SC} (mA cm $^{-2}$)	V_{OC} (V)	FF (%)	PCE (%)	Champion PCE (%)
No HTL	15.00 ± 2.00	12.57	0.68 ± 0.02	48.72 ± 7.23	5.01 ± 1.26	5.23
Li:PSS 0	16.84 ± 0.62	13.67	0.63 ± 0.05	55.63 ± 1.73	5.93 ± 0.55	6.87
Li:PSS A1	16.37 ± 0.57	16.50	0.61 ± 0.08	55.21 ± 8.41	5.50 ± 1.48	7.21
Li:PSS A4	16.79 ± 0.72	17.35	0.66 ± 0.06	57.15 ± 5.54	6.43 ± 1.13	7.96
Li:PSS A7	16.83 ± 0.78	17.46	0.73 ± 0.03	62.85 ± 4.91	7.73 ± 0.84	8.57
Li:PSS A10	17.17 ± 0.76	17.72	0.74 ± 0.01	65.17 ± 2.27	8.32 ± 0.44	8.99
Li:PSS M30	17.17 ± 0.82	17.87	0.73 ± 0.01	65.60 ± 2.27	8.33 ± 0.53	9.23
PEDOT:PSS	16.99 ± 0.76	14.47	0.73 ± 0.02	64.51 ± 2.85	8.09 ± 0.61	8.63

After 24 days, the PTB7 film on Li:PSS showed the smallest decrease in optical density (24.9% decrease), while films on ITO, H:PSS and PEDOT:PSS showed 32.7, 29.6 and 38.2% decreases in optical density over the same period. These results illustrate that PTB7 films deposited on pH-neutral, Li:PSS polyelectrolyte films are relatively stable compared to PTB7 films on ITO, H:PSS or PEDOT:PSS substrates.

Fig. 2a shows a schematic diagram representing the architecture of the solar cell devices used in this study (ITO/Li:PSS/PTB7:PC₇₁BM/PFN⁺Br⁻/Al) along with the chemical structure of Li:PSS. In this architecture, the active layer (PTB7:PC₇₁BM) absorbs sunlight to generate excitons, which separate into mobile electrons and holes *via* photoinduced electron transfer between PTB7 and PC₇₁BM.³ The PFN⁺Br⁻ ETL facilitates electron migration to the cathode (Al), while the HTL facilitates hole migration to the anode (ITO).

The $J-V$ curves for the best performing devices are shown in Fig. 2(b), and the average parameters, including standard

deviations, are summarized in Table 1. In addition, detailed photovoltaic performance both under simulated solar light and in the dark, and EQE spectra can be found in the ESI[†] (Fig. S2 and S3, respectively, ESI[†]). Reference devices without any HTL exhibited 5.01% efficiency with a short-circuit current density (J_{SC}) of 15.00 mA cm $^{-2}$, an open-circuit voltage (V_{OC}) of 0.68 V, and a fill factor (FF) of 48.71%. In contrast, a single layer Li:PSS layer showed an average PCE of 5.93% efficiency, including a J_{SC} of 16.84 mA cm $^{-2}$, V_{OC} of 0.63 and FF of 55.63%. The champion device was found to be the device using the Li:PSS M30 HTL; this device yielded a PCE of 8.33%, a J_{SC} of 17.17 mA cm $^{-2}$, a V_{OC} of 0.73, and a FF of 65.60%, as shown in Table 1. The device with Li:PSS A10 showed a similar efficiency of 8.32%, including a J_{SC} of 17.17 mA cm $^{-2}$, V_{OC} of 0.74, and a FF of 65.17%. The composition of Li:PSS A10 is a very close to that of Li:PSS M10, thus, it is not surprising that the Li:PSS M10 devices showed a similar performance including a PCE of 8.17%, as summarized in Table S2 of the ESI.[†]

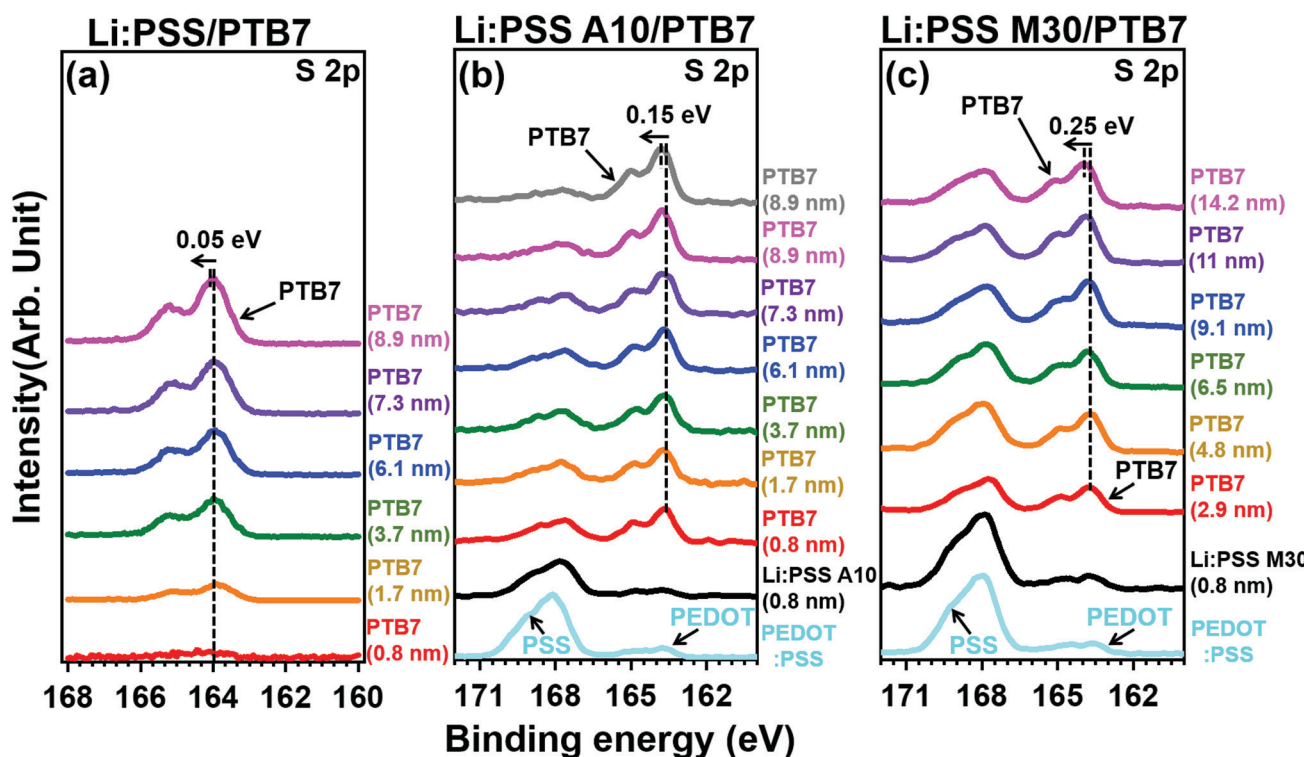


Fig. 3 XPS of S 2p spectra of PTB7 films with a different thickness deposited on top of (a) Li:PSS, (b) Li:PSS 10 and (c) Li:PSS 70 substrates.



EQE spectra corresponding to these devices are presented in Fig. 2c. The spectral J_{SC} values were calculated by integrating the area under the EQE curves and are also summarized in Table 1, with additional details in Table S2 and Fig S3 of the ESI.† The J_{SC} values of the devices with Li:PSS A10 and Li:PSS M30 HTLs were consistent with the spectral J_{SC} from EQE. However, the reference devices without HTLs and devices with ultra-thin neat Li:PSS films showed lower spectral J_{SC} values, which appears to have been due to sample degradation during EQE spectra acquisition. As checked in Table 1, even the devices with the pristine PEDOT:PSS decreased in spectral J_{SC} from 17.31 mA cm^{-2} to 14.47 mA cm^{-2} . Devices with Li:PSS 0, Li:PSS A10 and Li:PSS M30 HTLs had a peak at 390 nm, especially for the device with Li:PSS M30 reaching almost 80% as shown in Fig. S3 in the ESI.† The devices with Li:PSS A10 and Li:PSS M30 have an intermediate response in the range of 500 to 700 nm, with an average value of 64%. On the other hand, Li:PSS alone has a lower response with an average value of 60%.

In order to understand the influence of film morphology on the film properties, AFM was conducted. Surface topography images of the polyelectrolyte films are presented in Fig. 3 and more detailed topographic images including different scan sizes can be found in Fig. S4–S5 of the ESI.† All of the films showed relatively amorphous surface morphologies with no prominent structural features. These very thin Li:PSS films and Li:PSS A4 films have a surface structure similar to ITO itself.⁴⁰ The root mean square (RMS) of the surface roughness of all the films was in the range of 0.72 to 1.76 nm, which may be considered smooth enough for use as an HTL in solar cell devices. The neat Li:PSS films had an RMS roughness of 0.74 nm, while PEDOT:PSS alone had an RMS roughness of 1.06 nm and the roughness of the mixed films generally tended to be rougher with increasing PEDOT:PSS content.

Photoelectron spectroscopy including XPS and UPS were used to probe the chemical bonding states and electronic band structure of the films. Fig. 4 shows the sulfur 2p peaks in XPS for representative single layer Li:PSS, additive and mixture type

HTLs. Carbon peaks are shown in the ESI† (Fig. S6, ESI†) while changes in the secondary edge of the UPS spectra and the sulfur 2p peaks (XPS) can be seen in greater detail in Fig. S7(a) and (b), respectively (ESI†). The sulfur atom in the thiophene ring of PEDOT gives characteristic S 2p features between 162 and 166 eV while the sulfur atom in PSS occurs at 167.95 eV. Li:PSS alone shows only a strong peak at 168.75 (Fig. S7(b), ESI†). PEDOT:PSS shows both of these features, while representative Li:PSS, Li:PSS A10 and Li:PSS M30 films show relatively

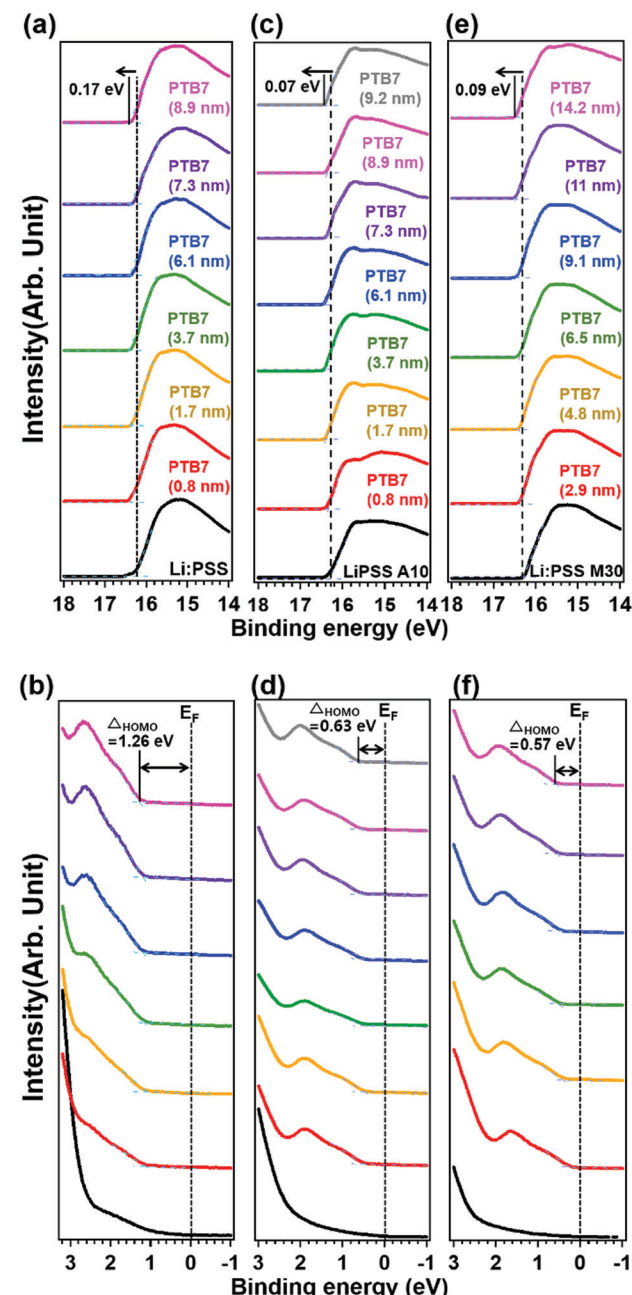


Fig. 5 UPS spectra for PTB7 films with different thicknesses on top of Li:PSS (a) and (b); Li:PSS A10 (c) and (d); and Li:PSS M30 (e) and (f) substrates. (a), (c), and (e) show the secondary edge while (b), (d), and (f) show the Fermi edge.

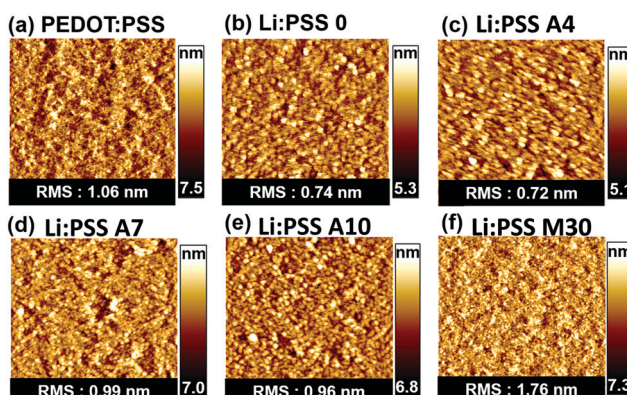


Fig. 4 Surface topographic AFM images (size: $5 \mu\text{m} \times 5 \mu\text{m}$) for (a) PEDOT:PSS, (b) Li:PSS, (c) Li:PSS 4, (d) Li:PSS 7, (e) Li:PSS 10, and (f) Li:PSS 70 films.



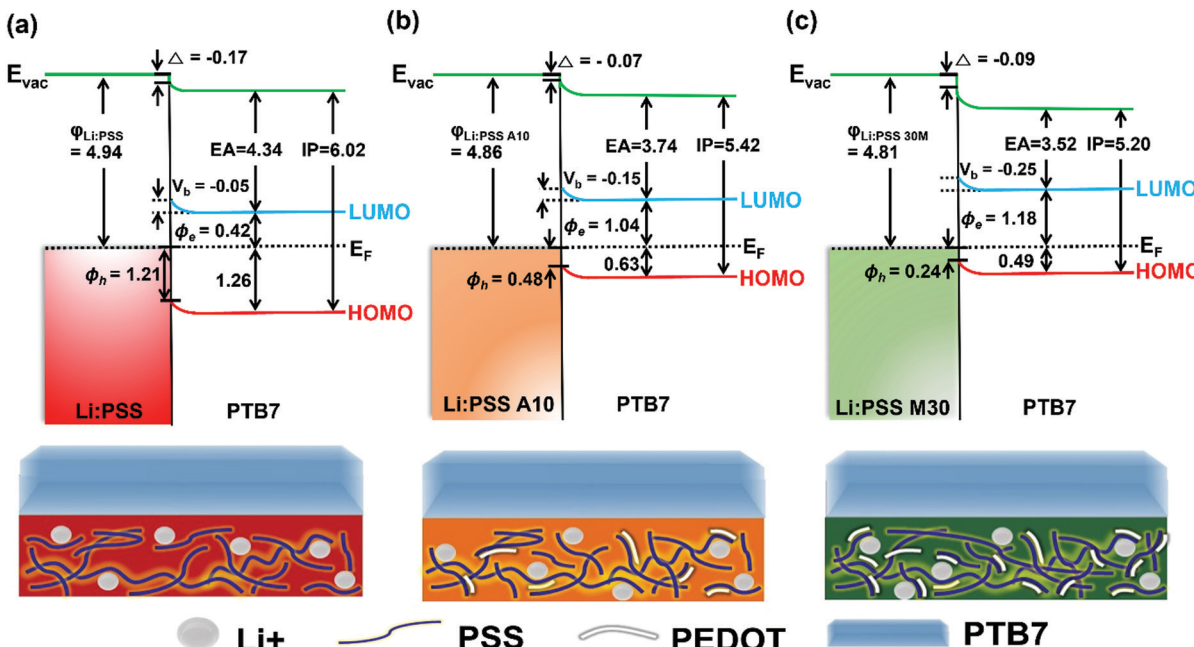


Fig. 6 Energy band diagrams for the anode interface with (a) Li:PSS, (b) Li:PSS A10, and (c) Li:PSS M30/PTB7.

stronger PSS features. PTB7 was deposited on top of the HTLs with incrementally increasing thickness to observe how the photoelectron spectra of PTB7 change going away from the HTL interface. As the PTB7 thickness increases from 2.9 to ~ 10 nm, the signals for the HTL become attenuated and the spectra become dominated by the strong thiophene signal generated by PTB7. Around 164 eV, corresponding to sulfur in thiophene rings, there are shifts in all devices as the PTB7 thickness increases. The neat Li:PSS devices showed only a 0.05 eV shift. Additionally, the additive and PEDOT:PSS rich mixtures exhibited 0.15 and 0.25 eV shifts to higher binding energy. These shifts also occurred in the C1s spectra (Fig. S6, ESI[†]) and indicate band-bending in the PTB7 phase at the HTL interface.

In Fig. 5, UPS spectra of the PTB7, Li:PSS, Li:PSS A10 and Li:PSS M30 samples are shown. The WF is the minimum energy required to extract an electron completely from the surface and is calculated by subtracting the secondary edge position (E_{SE}) from the incident photon energy ($WF = h\nu - E_{SE}$). The WFs of these devices assessed by UPS are 4.94, 4.86 and 4.81 eV, respectively. Also, by adding the WF and the highest occupied molecular orbital (HOMO) onset values, ionization potentials (IP) were calculated^{22,41} and found to be 6.02, 5.42 and 5.20 eV, for Li:PSS, Li:PSS A10 and Li:PSS M30, respectively. IP can be thought of as the distance between the vacuum level (E_{vac}) and the HOMO of the donor.²

The electron affinity (EA) is the energy released when an electron is added, and is located between the band edge of the lowest unoccupied molecular orbital (LUMO) level and E_{vac} . EAs for Li:PSS, Li:PSS A10 and Li:PSS M30 were found to be 4.34, 3.74 and 3.52 eV, respectively. The WFs of the HTLs were extracted from UPS analysis and calculated as 4.94, 4.86, and 4.81 eV for Li:PSS, Li:PSS A10, and Li:PSS M30, respectively.

HTLs that have high WFs are able to extract the electrons from the active layer effectively.⁴²

Energy band diagrams showing the band bending effect at Li:PSS/PTB7 interfaces were prepared using values extracted from XPS and UPS data as described above. These diagrams are shown in Fig. 6. The band-bending represents a decrease in the Fermi energy (E_F), and relative decrease (increase) in the equilibrium concentration of electrons (holes) in the PTB7 layer, which is representative of p-type doping.²²

Band-bending shifts (V_b) were confirmed by the shifts in the S 2p and C 1s XPS peaks at 164 eV and 284 eV, respectively (Fig. 4 and Fig. S6, ESI[†]). Fig. 4(a) shows that the Li:PSS S 2p peaks shifted by 0.05 eV to a higher binding energy, while in Fig. 4(b) and (c) Li:PSS A10 and Li:PSS M30 shifted by 0.15 and 0.25 eV, respectively. These increasing shifts in XPS spectra correlate with V_b . The interfacial dipole (Δ) value, which is calculated by the difference between WFs, increases with increasing V_b in devices. These features make a continuous transition between Li:PSS surfaces and the active layer, creating a permanent electric field near the anode which attracts holes while repelling electrons, the same type of band-bending that was expected using an anionic polyelectrolyte.⁴³ In addition to the band bending effect, hole injection barriers (ϕ_h) also determine the behavior of holes at the anode;^{44–46} where lower ϕ_h values are equivalent to lower energetic barriers to hole extraction and correlate to a higher current density in OSCs. The ϕ_h is the difference between the E_F and HOMO level. A minimum value of 0.24 eV was observed for the Li:PSS M30 HTL, as shown in Fig. 6(c). The ϕ_h of Li:PSS was found to be 1.21 eV and for Li:PSS A10 was 0.48 eV. Thus, as expected, Li:PSS M30 devices exhibited the lowest ϕ_h , and the strongest band bending effect, consistent with this HTL yielding the highest OSC performance.



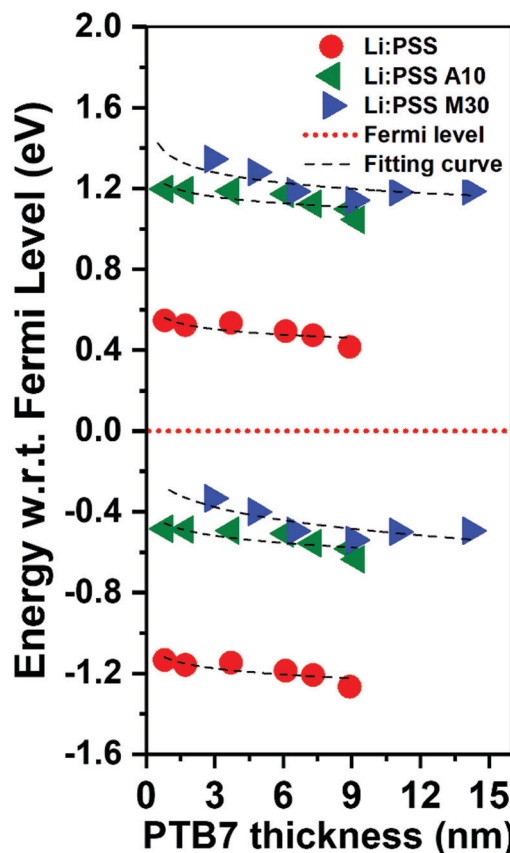


Fig. 7 Energy band structure relative to the Fermi level based on the changes in EA (top half) and IP (bottom half).

The energy change with respect to E_F and V_b can clearly be seen in Fig. 7 as the PTB7 film thickness increases away from the HTL interface. In this diagram, E_F is fixed at a value of 0 eV and the IP and EA (equivalent to valence and conduction band energies) are plotted relative to this at increasing distance from the HTL interface. The EA and IP for all HTLs slope downward away from the HTL interface, driving electrons to the right and holes to the left, equivalent to a p-doped junction. As the thickness of PTB7 increases, the Li:PSS electron injection barrier (Φ_e) drops to 0.42 eV, but the Φ_h increases, moving away from the E_F , to a value of 1.21 eV. Li:PSS A10 and Li:PSS M30, however, show a much larger Φ_e and much smaller Φ_h , together with greater slopes in the EA and IP. The values of Φ_e were determined to be 1.04 eV for Li:PSS A10 and 1.18 eV for Li:PSS M30, while the Φ_h remained low which was 0.48 eV for Li:PSS A10 and 0.24 eV for Li:PSS M30. In summary, the increased slope in IP, decreased Φ_h and increased Φ_e facilitate the drift of holes toward the anode, a small hole extraction barrier and an increased electron blocking effect, consistent with the highest device performance being observed in the Li:PSS A10 and Li:PSS M30 HTLs.

Conclusions

PEDOT:PSS is among the most widely used HTLs in the context of OSCs due to its relatively good performance as an HTL.

However, it's not clear how much the anionic polyelectrolyte component (PSS) contributes to its effect on the electronic band structure. This study sheds light on the relative role of the anionic PSS component through the investigation of the neutral polyelectrolyte Li:PSS and mixtures of Li:PSS with PEDOT:PSS as HTLs when used in combination with the benchmark organic active layer PTB7:PC₇₁BM.

We show that the anionic polyelectrolyte Li:PSS has an appreciable effect on the electronic band structure of PTB7 relative to no HTL. It causes a p-type band bending effect at the anode interface even without PEDOT, and moreover, can be mixed in various proportions with PEDOT:PSS, allowing the pH of mixtures to be adjusted from 1.2 for pure PEDOT:PSS through the range of 1.5 to 4.1 for mixtures of Li:PSS and PEDOT:PSS that show comparable or slightly improved performance compared to PEDOT:PSS alone. Using 2 nm thickness Li:PSS as a single layer HTL resulted in a PCE of 5.93%, while the performance in Li:PSS M30 and Li:PSS A10 mixtures was found to be 8.33% and 8.32%, respectively. Over time, we observed that the efficiency with these mixed HTLs did not decrease as much as PEDOT:PSS. Higher transparency is a desirable feature in the HTLs of OSCs,^{48,49} benefiting light transmission to the active layer.⁴⁷ Li:PSS has no visible absorption features (ESI,† Fig. S8), giving it ~3% higher transparency throughout the visible spectrum (250–800 nm) and less parasitic absorption than PEDOT:PSS. Additionally, Li⁺ has a lower ionic conductivity compared to H⁺, thus it may reduce instability due to ionic motion compared to PEDOT:PSS.⁵⁰ Furthermore, UPS and XPS studies revealed a reduction of Φ_h and p-type band bending effect which correlated with an increase in J_{sc} .^{37,44} These data shed light on the role that the anionic PSS polyelectrolyte plays in determining the electronic band structure of OSC devices and provides a route to decrease the acidity and improve the stability of HTLs.

Conflicts of interest

There are no conflicts to declare.

Acknowledgements

This research was supported by the National Research Foundation (NRF) of Korea (2017R1A2B2012971, 2019K1A3A7A09101449, 2020R1F1A1075539, 2021R1C1C2011757 and 2020H1D3A-1A02081526).

Notes and references

- 1 J. H. Seo, A. Gutacker, Y. Sun, H. Wu, F. Huang, Y. Cao, U. Scherf, A. J. Heeger and G. C. Bazan, *J. Am. Chem. Soc.*, 2011, **133**, 8416–8419.
- 2 S. Günes, H. Neugebauer and N. S. Sariciftci, *Chem. Rev.*, 2007, **107**, 1324–1338.
- 3 J. D. Servaites, M. A. Ratner and T. J. Marks, *Energy Environ. Sci.*, 2011, **4**, 4410.



4 G. Dennler, M. C. Scharber and C. J. Brabec, *Adv. Mater.*, 2009, **21**, 1323–1338.

5 M. C. Scharber and N. S. Sariciftci, *Prog. Polym. Sci.*, 2013, **38**, 1929–1940.

6 B. Walker, H. Choi and J. Y. Kim, *Curr. Appl. Phys.*, 2017, **17**, 370–391.

7 O. O. Amusan, H. Louis, S. Zafar, A. T. Hamzat and D. M. Peter, *Chem. Method.*, 2019, **3**, 425–441.

8 R. Bhargav, S. P. Gairola, A. Patra, S. Naqvi and S. K. Dhawan, *Opt. Mater.*, 2018, **80**, 138–142.

9 H. Xu, X. Fu, X. Cheng, L. Huang, D. Zhou, L. Chen and Y. Chen, *J. Mater. Chem. A*, 2017, **5**, 14689–14696.

10 H. Shi, C. Liu, Q. Jiang and J. Xu, *Adv. Electron. Mater.*, 2015, **1**, 1–16.

11 Y. Wen and J. Xu, *J. Polym. Sci., Part A: Polym. Chem.*, 2017, **55**, 1121–1150.

12 X. Fan, W. Nie, H. Tsai, N. Wang, H. Huang, Y. Cheng, R. Wen, L. Ma, F. Yan and Y. Xia, *Adv. Sci.*, 2019, **6**, 1900813.

13 X. Bao, J. Wang, Y. Li, D. Zhu, Y. Wu, P. Guo, X. Wang, Y. Zhang, J. Wang, H. L. Yip and R. Yang, *Adv. Mater. Interfaces*, 2017, **4**, 1–9.

14 Z. Li, Y. Liang, Z. Zhong, J. Qian, G. Liang, K. Zhao, H. Shi, S. Zhong, Y. Yin and W. Tian, *Synth. Met.*, 2015, **210**, 363–366.

15 Q. Wang, C. C. Chueh, M. Eslamian and A. K. Y. Jen, *ACS Appl. Mater. Interfaces*, 2016, **8**, 32068–32076.

16 K. M. Kim, S. Ahn, W. Jang, S. Park, O. O. Park and D. H. Wang, *Sol. Energy Mater. Sol. Cells*, 2018, **176**, 435–440.

17 B. Y. Kadem, M. Al-Hashimi, A. S. Hasan, R. G. Kadhim, Y. Rahaq and A. K. Hassan, *J. Mater. Sci.: Mater. Electron.*, 2018, **29**, 19287–19295.

18 L. Yin, Z. Zhao, F. Jiang, Z. Li, S. Xiong and Y. Zhou, *Org. Electron.*, 2014, **15**, 2593–2598.

19 L. M. Chen, Z. Hong, G. Li and Y. Yang, *Adv. Mater.*, 2009, **21**, 1434–1449.

20 T. Yang, M. Wang, C. Duan, X. Hu, L. Huang, J. Peng, F. Huang and X. Gong, *Energy Environ. Sci.*, 2012, **5**, 8208–8214.

21 L. Hu, M. Li, K. Yang, Z. Xiong, B. Yang, M. Wang, X. Tang, Z. Zang, X. Liu, B. Li, Z. Xiao, S. Lu, H. Gong, J. Ouyang and K. Sun, *J. Mater. Chem. A*, 2018, **6**, 16583–16589.

22 H. Zhou, Y. Zhang, C. K. Mai, S. D. Collins, T. Q. Nguyen, G. C. Bazan and A. J. Heeger, *Adv. Mater.*, 2014, **26**, 780–785.

23 A. Garcia, G. C. Welch, E. L. Ratcliff, D. S. Ginley, G. C. Bazan and D. C. Olson, *Adv. Mater.*, 2012, **24**, 5368–5373.

24 F. Xie, W. C. H. Choy, C. Wang, X. Li, S. Zhang and J. Hou, *Adv. Mater.*, 2013, **25**, 2051–2055.

25 K.-C. Wang, J.-Y. Jeng, P.-S. Shen, Y.-C. Chang, E. W.-G. Diau, C.-H. Tsai, T.-Y. Chao, H.-C. Hsu, P.-Y. Lin, P. Chen, T.-F. Guo and T.-C. Wen, *Sci. Rep.*, 2014, **4**, 4756.

26 C. Xia, W. T. Hong, Y. E. Kim, W.-S. Choe, D.-H. Kim and J. K. Kim, *Polymers*, 2020, **12**, 1791.

27 M. Ruscello, T. Sarkar, A. Levitsky, G. M. Matrone, N. Droseros, S. Schlisske, E. Sachs, P. Reiser, E. Mankel, W. Kowalsky, N. Banerji, N. Stingelin, G. L. Frey and G. Hernandez-Sosa, *Sustainable Energy Fuels*, 2019, **3**, 1418–1426.

28 S. Rafique, S. M. Abdullah, M. M. Shahid, M. O. Ansari and K. Sulaiman, *Sci. Rep.*, 2017, **7**, 1–10.

29 D. Romero-Borja, J. L. Maldonado, O. Barbosa-García, M. Rodríguez, A. de León, S. Fernández and E. Pérez-Gutiérrez, *Carbon*, 2018, **134**, 301–309.

30 S. Rafique, N. A. Roslan, S. M. Abdullah, L. Li, A. Supangat, A. Jilani and M. Iwamoto, *Org. Electron.*, 2019, **66**, 32–42.

31 L. Guguloth, K. Singh, V. S. Reddy Channu and K. Kumari, *Appl. Surf. Sci.*, 2021, **540**, 148266.

32 R. Bhargav, A. Patra, S. K. Dhawan and S. P. Gairola, *Sol. Energy*, 2018, **165**, 131–135.

33 R. Bhargav, N. Chaudhary, S. Rathi, Shahjad, D. Bhardwaj, S. Gupta and A. Patra, *ACS Omega*, 2019, **4**, 6028–6034.

34 M. S. G. Hamed, S. O. Oseni, A. Kumar, G. Sharma and G. T. Mola, *Sol. Energy*, 2020, **195**, 310–317.

35 A. Cominetti, G. Serrano, A. Savoini, C. Carbonera, F. Melchiorre, S. Perucchini, A. Congiu, G. Corso, R. Barbieri, E. Trippodo, A. Caneschi and R. Po, *Phys. Status Solidi A*, 2020, **217**, 1901023.

36 L. Wang, S. Zhao, Z. Xu, J. Zhao, D. Huang and L. Zhao, *Materials*, 2016, **9**, 1–9.

37 H. S. Jung and T. Q. Nguyen, *J. Am. Chem. Soc.*, 2008, **130**, 10042–10043.

38 J. H. Seo, R. Yang, J. Z. Brzezinski, B. Walker, G. C. Bazan and T. Q. Nguyen, *Adv. Mater.*, 2009, **21**, 1006–1011.

39 C. Nicollet, C. Toparli, G. F. Harrington, T. Defferriere, B. Yildiz and H. L. Tuller, *Nat. Catal.*, 2020, **3**, 913–920.

40 Y. J. Park, J. H. Seo, W. Elsawy, B. Walker, S. Cho and J. S. Lee, *J. Mater. Chem. C*, 2015, **3**, 5951–5957.

41 D. Shin, D. Kang, J. Jeong, S. Park, M. Kim, H. Lee and Y. Yi, *J. Phys. Chem. Lett.*, 2017, **8**, 5423–5429.

42 S. Park, J. Jeong, G. Hyun, M. Kim, H. Lee and Y. Yi, *Sci. Rep.*, 2016, **6**, 1–11.

43 J. H. Lee, J. H. Shin, J. Y. Song, W. Wang, R. Schlaf, K. J. Kim and Y. Yi, *J. Phys. Chem. C*, 2012, **116**, 26342–26348.

44 E. Knapp, R. Häusermann, H. U. Schwarzenbach and B. Ruhstaller, *J. Appl. Phys.*, 2010, **108**, 054504.

45 W. Yang, Y. Yao and C. Q. Wu, *Org. Electron.*, 2013, **14**, 1992–2000.

46 D. H. Wang, K. H. Park, J. H. Seo, J. Seifter, J. H. Jeon, J. K. Kim, J. H. Park, O. O. Park and A. J. Heeger, *Adv. Energy Mater.*, 2011, **1**, 766–770.

47 A. A. F. Husain, W. Z. W. Hasan, S. Shafie, M. N. Hamidon and S. S. Pandey, *Renewable Sustainable Energy Rev.*, 2018, **94**, 779–791.

48 D. H. Shin and S. H. Choi, *Coatings*, 2018, **8**, 329.

49 Y. Li, G. Xu, C. Cui and Y. Li, *Adv. Energy Mater.*, 2018, **8**, 1–28.

50 V. I. Volkov, A. V. Chernyak, D. V. Golubenko, V. A. Tverskoy, G. A. Lochin, E. S. Odjigaeva and A. B. Yaroslavtsev, *Membranes*, 2020, **10**, 272.

